# Cascaded Multilevel Active Rectifier Fed Three-Phase Smart Pump Load on Single-Phase Rural Feeder

Vishal Verma, *Member, IEEE*, and Amritesh Kumar

***Abstract*—Irrigation pumping system that marks a sizeable load on the grid is generally blind on assessment of peak demand hours, while in operation. Such operation if smartly controlled may avoid shedding of some connected loads to match power demand. Moreover, due to the accessibility of only single-phase supply, the rural pump three-phase loads are supplied through either by splitting ac single phase into three phases or by single phase ac–dc three-phase ac conversion. Such configuration suffers from power quality problems, higher capacitor voltages, and common mode voltage problems, etc. A seven-level cascaded multilevel active rectifier (CMAR) is proposed here to provide power through three different dc links to reduce the voltage rating of capacitors, feed vector-controlled open end winding induction motor pump in addition to variable illumination LED lighting. The control employed for CMAR enhances the grid support operation by flexibly controlling power on the dc links. The control is invoked by adjusting the speed of the pump by sensing the grid frequency using droop characteristics thereby acting as smart pump load. The effectiveness of the proposed configuration and control is investigated both through simulation and experimentation on same scale hardware prototype.**

***Index Terms*—AC–DC power conversion, induction motor drive, load management, multilevel systems power conditioning, phase conversion, smart pump load (SPL).**

## I. Introduction

THE economic prosperity of a developing country is gauged by the difference between electric power demand and supply. In developing countries, there always exist a gap between demand & supply and in the restructured power system major focus of utility companies is to cater the base loads while opting for demand management to stabilize their profits [1]. Due to high growth of manufacturing units and service industry the demanded load peaks at the certain time of the day which also vary seasonally and this poses a major problem before the utilities. Many-a- times to cater this peak demands some captive sources are used in addition to storage systems. Due to major constraints and the high cost of operation with captive sources, their utilization is also limited that affects severely the gap between demand and supply during peak times and often leads to frequency droop [2], [3].

Direct load control (DLC) has been advocated in literature for smartly controlling the loads in commercial/office buildings in urban areas thereby helping the utility to offset the financial burden and passively providing support to the grid stability [4]. DLC largely rely on the communication link between the buildings and the control centers. Wherein, for rural grids that are often used to cater many large/small pumps for irrigation purpose besides catering to rural domestic loads is so far neglected. All such loads act blindly and operate without any active interaction with the grid, which in a case is participated for demand side management with the grid can reasonably avert the peaking of demand [5].

A major part of the total energy being utilized in rural areas includes the conventional single-phase induction motor for water pumping application in agriculture sector due to the availability of single-phase supply in far flung areas, knowingly that, such motors are highly inefficient as compared to three-phase induction motors [6]. The three-phase induction motor pumps fed from single phase using passive elements are reported, but such configuration often lead to improper phase displacement due to shorter life of capacitor, which adversely affect the motoring operation [7]. To avert such situation, the single- phase ac–dc three-phase ac conversion has been advocated, which maintain a steady excitation of the machine indifferent to the frequency changes in the grid. Converter– Inverter variable voltage variable frequency (VVVF)-based drives have been recently advocated specially for submersible pumping operation with enhanced efficiency and better throughput and accordingly three-phase induction motor drive fed from single-phase power supply have been reported in the literature [8], [9]. The reported literature also utilizes half-bridge configuration for active rectification by sacrificing the dc link voltage which becomes half, apart from an advantage of the lesser number of switches [10], whereas another literature has suggested full bridge configuration [11]. The major issues with VVVF drive lie with the requirement of high-value capacitor on the dc link. Such electrolytic capacitors are very sensitive to heat, and its lifetime reduces to half on every 10° rise in temperature at higher voltages [12].

The dynamics and transient response of the drive (inverter–motor pump system) depend on the techniques used for the drive control. Recently, in literature v/f controlled open end winding induction motor (OEIM) for photovoltaic pumping application

Manuscript received August 30, 2015; revised June 15, 2016; accepted August 4, 2016. Date of publication August 31, 2016; date of current version February 27, 2017. Recommended for publication by Associate Editor L. Zhang.

The authors are with the Department of Electrical Engineering, Delhi Technological University, Delhi110042, India (e-mail: amritesh@dce.ac.in; vishalverma@dce.ac.in).

Color versions of one or more of the figures in this paper are available online at http://ieeexplore.ieee.org.

Digital Object Identifier 10.1109/TPEL.2016.2605005

using DSAZE algorithm is reported [13]. The major problem with constant v/f control drive lies with its coupled real and reactive component that makes response sluggish and may lead to over fluxing of the motor leading to heating of the motor. On the other hand, the vector-controlled drive for the induction motor finds application for fast dynamics and transient free operation as compared to constant v/f drive [14]. Further, the conventional drive operation with common single high dc bus suffers from a problem of high dv/dt stress, common mode voltage (CMV) and leakage current [15]. To reduce such CMV, OEIM drive using single common dc source with a space vector modulation technique is reported [16]. Others have also proposed OEIM drive with separate dc source using dual bridge configuration to avoid the problem CMV and zero sequence current [17]. The reported drive configurations utilizing three-phase bridges employing single high dc link capacitor, under sudden supply disconnection, prevalent on rural grid may induce high line voltage across the stator windings due to high di/dt generated by arrest of the rotor causes high stresses on the capacitor too, resulting in reduced life of the drive [18]. The situation further deteriorates for pump drive being an active load, as the air gap flux dies out very fast. This necessitates the probe on such configurations that could reduce these stresses by distributing them in different winding and /or on the capacitors.

Moreover to act as a smart pump load (SPL), such structure should be ready to be integrated with renewable energy sources to minimize the dependency on the grid and thereby participating in wide range of demand side management. The proposed multilevel structure thus typically suits majority requirements for smart pumping operation interacting with grid frequency to yield variable speed operation. However, voltage balancing remains a challenge for the proposed structure to present balanced condition before OEIM drive. The problem to balance the voltage in dc links became graver while dealing with transient and intermittent operation, which otherwise may lead to very large unbalance in voltages [19]. In the reported literature, control techniques such as power balance control and passivity-based control are generally used to balance the dc buses [20]. Recently in the literature, variable switching-based pattern is also reported to avoid voltage imbalances at the cost of poor THD in voltage on ac side [21]. Others methods of dc voltage balancing for improved THD operation using selective harmonic elimination for cascaded multilevel, etc., are also researched and reported [22], [23].

In this paper, a novel structure of SPL represented for autonomous variable speed pumping system with single-phase grid connectivity is presented. The variable speed pumping system is facilitated by seven-level cascaded multilevel active rectifier (CMAR) feeding three dc links working as one end of the back to back connected H-bridges, in turn forming three-phase connection to operate the pump as vector-controlled OEIM drive. With the new proposed structure for SPL, the problem of the conventional and noninteractive pumping system can be easily circumvented due to the structure and its flexible control for variable pump load with reduced dc link capacitor size. Further, due to division of voltage along the three dc links any stress from grid side will also get distributed on the split dc links, leading to increased lifetime of the capacitor and

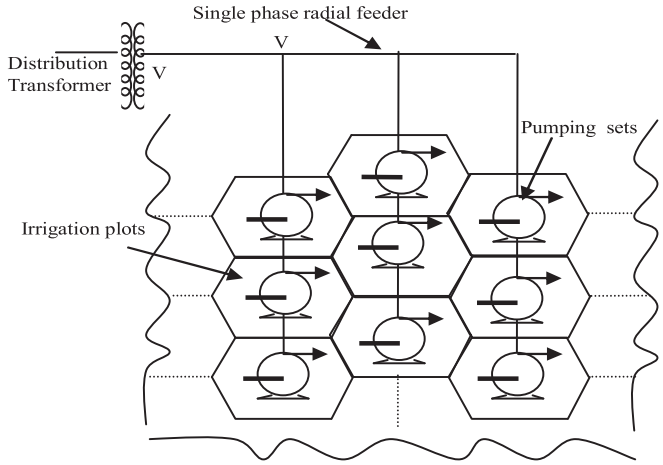


Fig. 1. Conventional system of pumping.

the drive. Such variable speed SPL that operates as per variation in grid frequency by controlling the power drawn from the ac mains. When the demand peaks up during a day, sensing the grid frequency, the droop characteristics dictates the power drawn through the SPL and the same is matched by an appropriate reduction in the speed of the pump load. For the proposed control applied to the SPL, the droop rate is decided based on the prevailing grid frequency and the individual capacity of the pump drive load. When the CMAR is also feeding variable illumination LED (VIL) on the dc link, the control is then altered according to the droop rate considering the net reduction in equivalent loads on dc links and the decrease/increase in speed resulting in increase/decrease in power demand from grid to stabilize the grid frequency. In rural areas with many such proposed connected SPL, the grid will be more stabilized and load shedding would be in turn averted. The lab prototype of the proposed SPL unit is developed and integrated with sensors, interfacing circuits, driver, etc., for real-time implementation. The performance of the system is analyzed through simulation and experimental results, which demonstrate the effectiveness of proposed control and stability of configuration.

## II. System Configuration

Fig. 1 depicts a broader view of linked problem associated with connectivity of array of pumps used for irrigation on a single-phase distribution system. Fig. 2 shows the proposed SPL connected to a 240-V, 50-Hz single-phase ac input. The SPL is composed of both, open end winding three-phase variable speed induction motor pump (1 Hp, 200 V) and other VIL loads (960 W at 150 V) connected to three separate dc links of CMAR. The SPL transacts power through active rectifier in cascaded multilevel mode creating three dc links which in turn feeds three independent H-bridges to vector control the OEIM pump load. Each of the three smaller dc links hosts a common dc link capacitor between the rectifier and inverter bridges. The SPL is interfaced with single-phase grid via interface inductor, which helps in controlling the power transaction from the grid. On each of the three separate dc links, three independent VIL loads ($R_1$, $R_2$, $R_3$) are connected depicted by variable duty

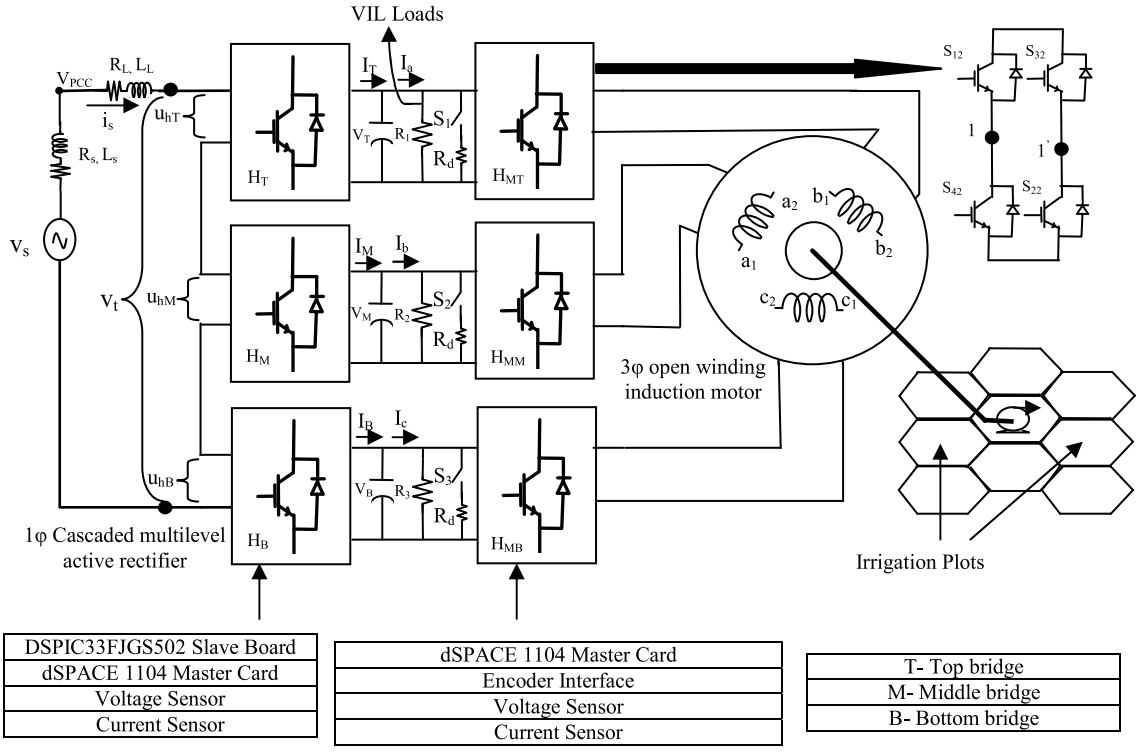


Fig. 2. Proposed system configuration for SPL operation.

cycle passive loads to additionally create a scope of unbalance loading to test the effectiveness of the algorithm against each of the odd situations. Load controllers are also connected to the dc links for protection and to avert any case of transient overvoltage arising due to switching on/off of dynamic load. The three dc links so created feeds vector-controlled OEIM pump drive, where individual H-bridges act as power modulators. The overall power drawn by the SPL and another VIL depends on the prevailing grid frequency conditions. The different loads attached with the dc links are smartly altered to draw adequate power from the grid dictated by grid frequency. The alteration of power drawn is ranged by the value of interface inductor (6 mH, assuming 10% ripple component in the inductor current), which is connected between 240-V ac grid and SPL [24]. The rating of capacitor on each dc link is decided on the basis of the allowable voltage ripple and power exchange [25].

## III. CMAR Switching Technique

For seven-level operation of CMAR, the phase shifted modulation technique is used [26]. To form the seven-level terminal voltage through the CMAR six carrier signals displaced by 60° each is compared with reference modulating sine wave signal to provide the pulse width modulation (PWM) signals for three H-bridge. An example to such, under balanced loading condition, is shown in Fig. 3(b). Utilizing the switching signals so generated and output of each H-bridge so obtained [shown in Fig. 3(c)], the cascaded connection yields seven-level terminal voltages as shown in Fig. 3(c). Decreasing the modulation index ($m_j$) in turn increases the inward power flow, but such overload may lead to the reduction in the levels of terminal voltage from 7 to 5, as also depicted from 1.78 s onwards in Fig. 3(a).

## IV. SPL Management Control

The power flow from the grid is governed by power angle between point of common coupling ($V_{\rm PCC}$) and terminal voltage ($V_t$), which in turn is controlled by modulation index for operation of individual bridges of CMAR. Hence, the decrease in power flow shall be marked by increase in modulation index, directing the control for reduction in the speed of SPL. Thus, the decision of selection of modulation indices should be duly governed in respect of grid capacity (freq≥50 Hz, power surplus or freq ≤50-Hz power deficient). During power surplus condition, the modulation indices get decided as per predefined reference values of speed of SPL unit. Whereas for deficient power condition, SPL prompt for slower speed as commanded by the droop characteristics, directing the changes to control for alteration in the modulation indices. The cumulative autonomous efforts of multiple SPL on the rural feeder smartly reduce the power burden and contribute towards stability and frequency restoration on the grid. The droop characteristic of individual SPL is considered in conformance with individual power capacity of the pump load. The slope for the droop rate bounded by critical limits of the frequencies can be expressed as (shown in Fig. 4(a):

$$\tan\alpha = \frac{f_{\rm rated} - f_{\rm critical}}{P_{\rm rated} - P_{\rm critical}} \tag{1}$$

where $f_{\rm rated}$ and $P_{\rm rated}$ are rated frequency and rated power, respectively, and $f_{\rm critical}$ and $P_{\rm critical}$ reflect the critical frequency of the reference grid (decided on the basis of installed capacity by the regulator) and the critical power (beyond which the SPL should be disconnected for the grid support), respectively.

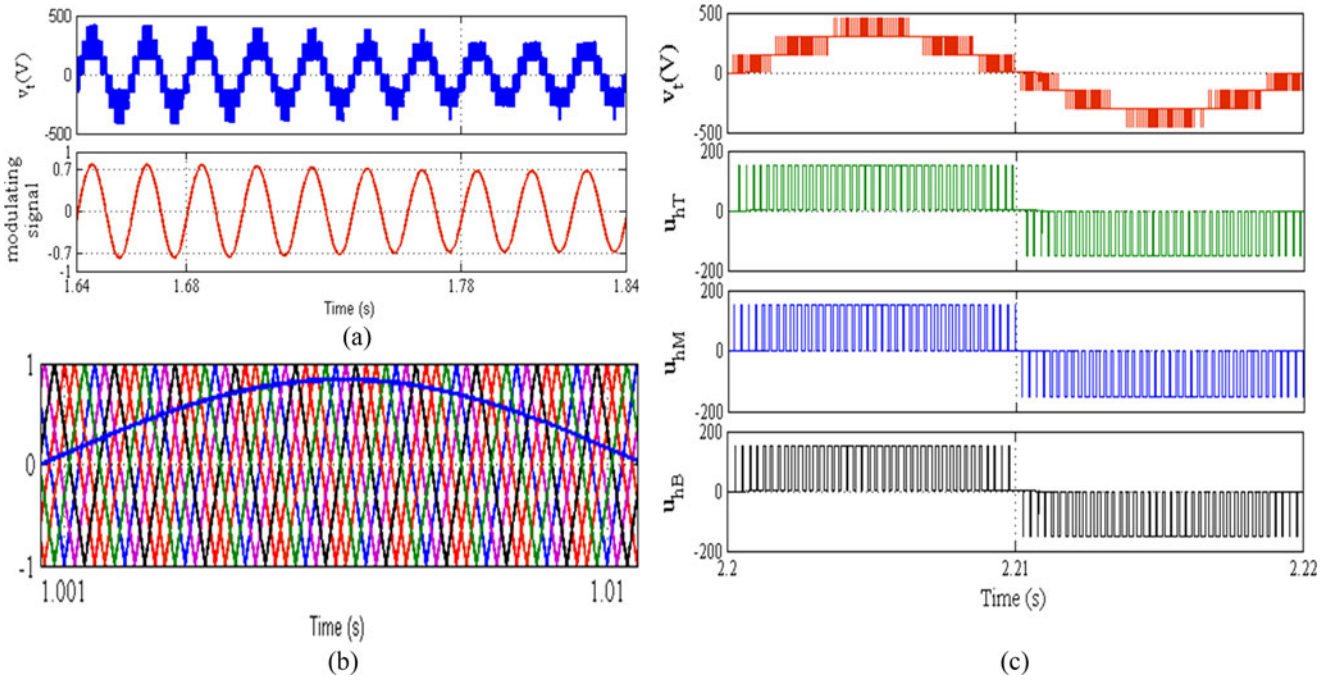


Fig. 3. (a) CMAR response under varying modulation index. (b) CMAR control operation with phase shifted modulation technique. (c). CMAR instantaneous each H-bridge terminal voltage contributing toward formation of seven-level multilevel converter.

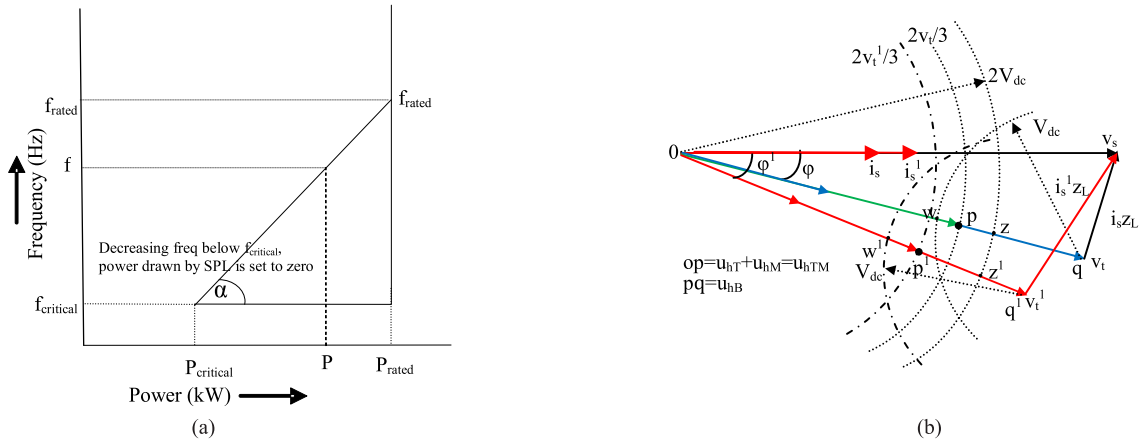


Fig. 4. (a) Droop curve according to individual capacity of pump load. (b) Phasor diagram representing UPF and operating region with changing loading condition.

Similarly, the expression for relationship between power and frequency may be expressed as follows:

$$f - f_{\text{rated}} = \tan\alpha \times (P - P_{\text{rated}}). \tag{2}$$

Substituting the value of tan $\alpha$ from (1) in (2), the power drawn from the grid at any frequency can thus be suitably estimated as follows:

$$P = P_{\text{rated}} + (f - f_{\text{rated}}) \times \frac{P_{\text{rated}} - P_{\text{critical}}}{f_{\text{rated}} - f_{\text{critical}}}. \tag{3}$$

Since the rural load approximately comprise 60–70% pump load [27], if controlled smartly, reduce the power consumption, and aid to the restoration of the grid frequency. The quantum of frequency restoration will depend on the capacity of grid and number of units of SPL connected to the grid. As per Central Electricity Regulatory Commission, India, the critical frequency ($f_{\text{critical}}$) is fixed to 49.5 Hz [28]. The power to be drawn by CMAR in consonance with (3) is required to be shared between VIL and SPL as follows:

$$P = P_{\text{VIL}} + P_{\text{SPL}}. \tag{4}$$

For constant voltages maintained on the dc links the (4) may be modified as follows:

$$P = {V_{\text{dc}}}^2 \sum_{j=1}^{3} \left(\frac{1}{R_j}\right) + K_m {\omega_r}^3 \tag{5}$$

where $V_{\rm dc}$ is common dc link voltage ($V_T = V_M = V_B = V_{\rm dc}$), $R_j$ ($j = 1, 2, 3$) is the equivalent resistance (VIL) seen on individual dc links, $K_m$ is motor constant and $\omega_r$ is motor speed. Thus, from expression (5), it is clear that the power (P) estimated through the droop curve is controlled mainly by decreasing /increasing the speed of the SPL to match the power estimated through the droop curve as in the day time (peak demand hour) when the lighting loads will be in OFF state. In the night time when the supply is surplus to feed both the VIL load and SPL, both shall operate at the fullest capacity. Only in critical cases, typically in the evening the VIL may also be altered by changing the illumination to match the power dictated by droop characteristics, while the pump is being operated at lowest critical speeds.

## V. Phasor Analysis for Unity Power Factor (UPF) Operation at Balanced Loading Condition

For individual H-bridges ($H_T$, $H_M$, $H_B$) shown in Fig. 2, the power is drawn by each H-bridge is given by

$$P_j = u_{\rm hj} \cdot i_s \tag{6}$$

where $u_{\rm hj}$ (*j* is *T*, *M*, *B*) is the terminal voltage of individual H-bridges, and $i_s$ is the source current common to all H-bridge.

Further, the component of real power drawn by individual bridges is given as follows:

$$P_{j,\rm real} = U_{\rm hj} I_s \cos(\theta_j). \tag{7}$$

$U_{\rm hj}$ is the rms value of individual bridge, $I_s$ is the rms value of current common to all the H-bridges, and $\theta_j$ ($\theta_j$ equal to $\varphi$ under balanced loading on each dc link) is the power factor angle between the fundamental frequency source current ($i_s$) and the terminal voltage ($u_{\rm hj}$) of each bridge, respectively. This will also be the power angle ($\varphi$) for UPF operation of CMAR under uniform balanced loading. Moreover, for the balanced loading condition on dc links, $\theta_j$ will be the same for all the three bridges. Hence, for balanced loading conditions alteration in power is equally shared by each bridge by changing both individual bridge terminal voltage with equal power factor angle $\theta_j$ (angle will get altered with load changes) through a change in modulation index for UPF operation.

To make the illustration more lucid, a phasor diagram for UPF operation under balanced loading conditions having equal dc link voltage and the same $\theta_j$ (equal to $\varphi$) for each bridge is shown in Fig. 4(b). The terminal voltage phasor ($v_t$) in Fig. 4(b) is divided into two parts of magnitude $(m_T + m_M)V_{\rm dc}$ and $m_B V_{\rm dc}$ and the point of operation (*p*) of cumulative two bridges with respect to the third bridge is shown identifiable through the corresponding arcs. The arcs corresponding to $2V_{\rm dc}$ and $V_{\rm dc}$ intent to explain an overlapping area, which encloses this point conforming to the feasibility of operation. Any mismatch in loading during transient operation will dislodge the point "*p*." If this displacement is within the overlapping area, it can be reinstated by appropriately controlling the modulation indexes of the bridges for UPF operation with balanced loading conditions. Accordingly, the section pz: pw will be reinstated to 2:1 ratio.

Even with changed balanced loading condition under UPF operation, the ratio of 2:1 has to be always maintained. To make a presentation of phasor and its range of operation in terms of $m_j$ lucid in Fig. 4(b) for UPF operation, decreased modulation index (decrease in $v_t$), and increase in power angle represented as oq$^1$ ($v_t^1$) and $\varphi^1$, respectively, as shown for increased balanced loading condition on individual H-bridges. This resulted into changed operating points ($p^1$) bounded by arcs $2V_{\rm dc}$, $2m_j^1 V_{\rm dc}$, and $m_j^1 V_{\rm dc}$, where $m_j^1$ is the new modulation index of individual H-bridges (*j* is *T*, *M*, *B*). As evident from phasor diagram, the increased loading resulted into the wider scope of handling unbalance on individual H-bridge. The details of the same will be discussed in next section. Further decrease in modulation index, beyond the critical value may cause a change in the levels of terminal voltage from 7 to 5, as, beyond the critical limit, the modulation indices are not sufficient enough to enable simultaneous utilization of three individual H-bridges as evident from Fig. 3(b). This may lead to deterioration in the power quality (PQ) at the PCC. So to have improved PQ operation, the region of control for the modulation index is made between $0.7 < m_j < 1$.

## VI. CMAR Mathematical Modeling and Control Theory of CMAR and DC Link Balancing Scheme

### A. CMAR Mathematical Modeling

The schematic of CMAR as shown in Fig. 2 may be expressed in terms of set differential equations as follows:

$$\frac{di_s}{\rm dt} = \frac{1}{L_L}\left(v_s - i_s R_L - m_T v_T - m_M v_M - m_B v_B - 3R_{\rm switch} i_s\right) \tag{8}$$

$$\frac{dV_T}{\rm dt} = \frac{1}{C}\left(\frac{i_s m_T}{\sqrt{2}} - I_a\right) \tag{9}$$

$$\frac{dV_M}{\rm dt} = \frac{1}{C}\left(\frac{i_s m_M}{\sqrt{2}} - I_b\right) \tag{10}$$

$$\frac{dV_B}{\rm dt} = \frac{1}{C}\left(\frac{i_s m_B}{\sqrt{2}} - I_c\right) \tag{11}$$

where $i_s$ is source current, $v_s$ is the PCC voltage, $L_L$ is the interfacing inductor, $R_L$ is the inductor resistance, $R_{\rm switch}$ represents the losses across each H-bridge, $m_i$ (where *i* is *T, M,* and *B*) represents modulation index of corresponding bridge; $I_j$ (where *j* is *a,b,c*) is load current at individual dc link,$V_i$ (*i* is *T*, *M*, *B*) is the dc link capacitor voltage. Using (8)–(11), the average model of CMAR can be modeled in the matrix form as follows:

$$\frac{d}{\rm dt}\begin{bmatrix} i_s \\ v_T \\ v_M \\ v_B \end{bmatrix} = \begin{bmatrix} \frac{-(R_L + 3R_{\rm switch})}{L_L} & 0 & 0 & 0 \\ 0 & 0 & 0 & 0 \\ 0 & 0 & 0 & 0 \\ 0 & 0 & 0 & 0 \end{bmatrix} \begin{bmatrix} i_s \\ v_T \\ v_M \\ v_B \end{bmatrix}$$

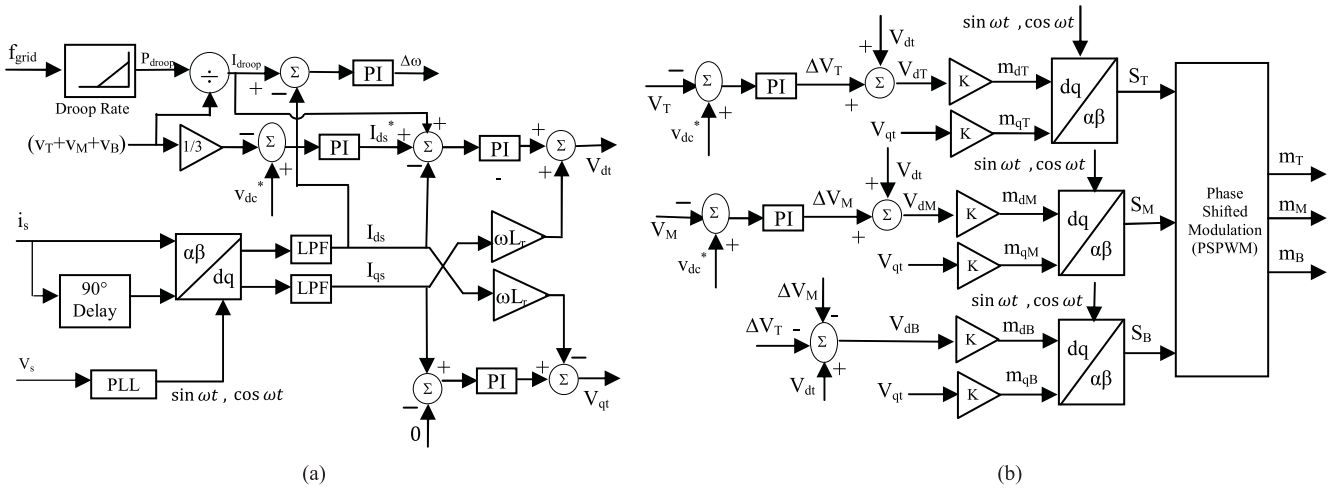


Fig. 5. (a) Control blocks of proposed CMAR + SPL configuration. (b) Control blocks of proposed SPL + CMAR configuration for switching function generation for each H-bridge incorporating control block set for handling unbalanced loading.

$$+\begin{bmatrix} \frac{-v_T}{L_L} & \frac{-v_M}{L_L} & \frac{-v_B}{L_L} & 0 \\ \frac{i_s}{\sqrt{2}C} & 0 & 0 & 0 \\ 0 & \frac{i_s}{\sqrt{2}C} & 0 & 0 \\ 0 & 0 & \frac{i_s}{\sqrt{2}C} & 0 \end{bmatrix} \begin{bmatrix} m_T \\ m_M \\ m_B \\ 0 \end{bmatrix}$$

$$+\begin{bmatrix} \frac{1}{L_L} & 0 & 0 & 0 \\ 0 & \frac{-1}{C} & 0 & 0 \\ 0 & 0 & \frac{-1}{C} & 0 \\ 0 & 0 & 0 & \frac{-1}{C} \end{bmatrix} \begin{bmatrix} v_s \\ I_a \\ I_b \\ I_c \end{bmatrix}. \quad (12)$$

### B. Control Theory of CMAR and DC Link Balancing Scheme

After making an estimate of the total power to be drawn by CMAR unit with the help of droop characteristics, the individual power to be drawn by each H- Bridge under balanced/unbalanced loading has to be is directed through proper control algorithm. In the absence of incorporation of different $\theta_j$ and $m_j$ for different H-bridges under uneven loading condition on different dc links, the H-bridges are forced to draw unequal power from the mains for the same source current. This may lead to different voltages at the different dc links. So, for balancing the dc link voltages, the modulation of individual H-bridges has to be changed to accommodate the load demand. For precise determination of $\theta_j$ and $m_j$, components for each H-bridge necessitate the operation in the synchronous reference frame theory (SRF) frame to get the decoupled components for individual bridges. Fig. 5(a) and (b) depicts the complete control logic for control of individual H-bridges with balanced/unbalanced loading on dc links. For the present control, SRF-based control has been designed for referencing all the ac quantities into dc using park transformation and utilizing unit vector (cos $\omega$t, sin $\omega$t). The source current vector and its delayed (90°) component is used to obtain $i_\alpha$ and $i_\beta$ represented as [29] follows:

$$i_s = i_\alpha = A.\sin\omega t \quad (13)$$

$$i_\beta = A.\sin\left(\omega t - \frac{\pi}{2}\right), \text{ where } A \text{ is amplitude .} \quad (14)$$

Further using park transformation the *d–q* components are computed as follows:

$$\begin{pmatrix} i_{\rm ds} \\ i_{\rm qs} \end{pmatrix} = \begin{pmatrix} \sin\omega t & -\cos\omega t \\ \cos\omega t & \sin\omega t \end{pmatrix} . \begin{pmatrix} i_\alpha \\ i_\beta \end{pmatrix}. \quad (15)$$

With SRF-based control, the decoupled control of real and reactive power is easily implemented. From (15), it is clear that $i_{\rm ds}$ represent the active power component and $i_{\rm qs}$ represents the reactive power component under the assumption of constant bus voltage at PCC. From Fig. 5, it is clear that reference source current ($i^*_{\rm ds}$) is derived by comparing the averaged dc link voltage of individual H-bridges with reference voltage. But due to varying power demand by individual bridges the power demanded at each H-bridge may be expressed in *d–q* frame as follows:

$$P_j = \frac{i_{\rm ds}}{2}\ (V_{\rm dj} - jV_{\rm qj}) \quad (16)$$

where $P_j$ (where *j* is *T, M, B*) is the power demanded and $V_{\rm dj}$, $V_{\rm qj}$ is the voltage in *d–q* frame of the corresponding H-bridge.

So total power demanded by 3 H-bridges is expressed as follows:

$$P_{\rm demanded} = P_T + P_M + P_B = \frac{i_{ds}}{2}\left[V_{\rm dt} + V_{\rm dM} + V_{\rm dB} - j\left(V_{\rm qt} + V_{\rm qM} + V_{\rm qB}\right)\right]. \quad (17)$$

And power supplied through the input terminal is given by

$$P_{\rm supplied} = \left(V_{\rm dt} - jV_{\rm qt}\right)\frac{i_{ds}}{2} \quad (18)$$

where $v_t = (V_{\rm dt} - jV_{\rm qt})$ terminal voltage as shown in Fig. 1.

For power balanced operation (neglecting the power losses occurring in the system), the equation may be expressed as follows:

$$P_{\rm supplied} = P_{\rm demanded} \quad (19)$$

$$(V_{\rm dt} - jV_{\rm qt})\,\frac{i_{\rm ds}}{2} = \frac{i_{\rm ds}}{2}\;[V_{\rm dt} + V_{\rm dM} + V_{\rm dB} - j\,(V_{\rm qt} + V_{\rm qM} + V_{\rm qB})] \tag{20}$$

where $V_{\rm dt}$ and $V_{\rm qt}$ can be expressed as follows:

$$V_{\rm dt} = V_{\rm dt} + V_{\rm dM} + V_{\rm dB} \tag{21}$$

$$V_{\rm qt} = V_{\rm qt} + V_{\rm qM} + V_{\rm qB}. \tag{22}$$

Moreover, terminal voltage can be expressed in terms of source voltage and drop across inductor in *d–q* reference frame as:

$$V_{\rm dt} = -L_L\frac{di_{\rm ds}}{\rm dt} + L_L w i_{\rm qs} + V_{\rm ds} - i_{\rm ds}\,(R_L + 3R_{\rm switch}) \tag{23}$$

$$V_{\rm qt} = -L_L\frac{di_{\rm qs}}{\rm dt} - L_L w i_{\rm ds} + V_{\rm qs} - i_{\rm qs}\,(R_L + 3R_{\rm switch}). \tag{24}$$

Neglecting the losses across the bridges and in the interface inductor ($R_L + 3\,R_{\rm switch} = 0$); substituting $V_{\rm qs} = 0$ (as $v_s$ is synchronized with sin $\omega$t obtained through PLL) and $i_{\rm qs} = 0$ (for UPF), (23) and (24) may be written as follows:

$$V_{\rm dt} = -L_L\frac{di_{\rm ds}}{\rm dt} + V_{\rm ds} \tag{25}$$

$$V_{\rm qt} = -L_L w i_{\rm ds}. \tag{26}$$

Substituting value of (25) in (21), and rewriting (25) as follows:

$$L_L\,\frac{di_{\rm ds}}{\rm dt} = V_{\rm dt} + V_{\rm dM} + V_{\rm dB} - V_{\rm ds}. \tag{27}$$

Dividing both sides by $V_{\rm dc}$ to probe the relation for modulation indices (assuming $V_T = V_M = V_B = V_{\rm dc}$), may be written as follows:

$$\frac{L_L}{V_{dc}}\cdot\frac{di_{ds}}{\rm dt} = \frac{1}{V_{\rm dc}}\,(V_{\rm dt} + V_{\rm dM} + V_{\rm dB} - V_{ds}) = (m_{\rm dt} + m_{\rm dM} + m_{\rm dB} - \frac{V_{\rm ds}}{V_{\rm dc}}). \tag{28}$$

Similarly substituting (26) in (22) and dividing both sides by $V_{\rm dc}$, (26) may be written as follows:

$$\frac{\omega L_L i_{\rm ds}}{V_{\rm dc}} = m_{qT+}m_{\rm qM} + m_{\rm qB}. \tag{29}$$

For a stable region of operation of CMAR, (28) and (29) have to be always satisfied irrespective of the loading conditions at the individual H-bridges.

For either balanced/unbalanced loading condition of individual H-bridges, the overall power drawn by CMAR is determined through magnitude and power angle ($\varphi$) of the overall terminal voltage phasor ($V_t$) as shown in Fig. 6. The distribution of terminal voltage of individual H-bridges under unbalanced loading will be distributed nonuniformly depending on power to be handled by each bridge. The distribution may only guarantee the equal dc link voltages of H-bridges with appropriate modulation index. For tackling such unbalanced situation, the individual dc link voltages are compared with the reference voltage and the error is passed through PI controller to add voltage ($\Delta V_j$)–$V_{\rm dt}$ as shown in control diagram Fig. 5(b). Only two PI

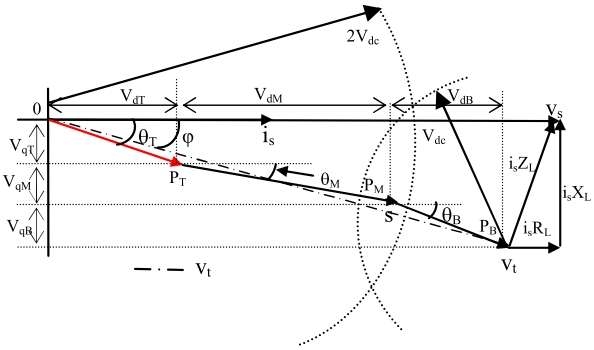


Fig. 6. Phasor representation of individual voltages in case of unbalanced loading.

controllers are required to formulate the control for balancing the dc link voltage since third output may derive from output of two PI's controllers with overall change in voltage as zero ($\Delta V_B = -(\Delta V_T + \Delta V_M)$ as shown in control Fig. 5(b). Since the H-bridges are connected in series, the same current will be drawn by them, thus, to accommodate the unbalance power requirement, the terminal voltage phasor of individual H-bridge voltage ($P_j$ – where *j* is *T*, *M*, *B*) should be of varying magnitude due to different modulation indexes of individual H-bridges. So from control, it is evident that unbalance power requirement is fulfilled by changing the modulation indices $m_{\rm dj}(j - T, M, B)$, which leads to change in magnitude of *d*-axis voltage component ($V_{\rm dj}$). Since the reference voltage along the *q*-axis is divided uniformly along the H-bridge for UPF operation, the individual H-bridge power factor angle ($\theta_j$) depends on the magnitude of *d*-axis voltage component ($V_{\rm dj}$) which in turn depends on loading condition, i.e., higher the terminal voltage ($V_{\rm dj}$) of the H-bridge will require higher modulation index leading to smaller power factor angle and, therefore, more real power will be drawn by the particular H-bridge as shown in Fig. 6. Such customized modulation index guarantees the operation of the H-bridges with equal dc link voltages irrespective of the loading condition at each bridge amid load perturbation /disturbances on the grid.

Transforming these individually controlled variable ($m_{\rm dj}$, $m_{\rm qj}$) from *d–q* to $\alpha$–$\beta$ frame using reverse park transformation and computing individual switching function as $S_j$ (where *j* is *T, M, B*), which is further being used as an input for phase shifted modulation (PSPWM) to generate individual H-bridge gating pulses.

## VII. Modeling and Control of Open Winding Induction Motor

Three-phase induction motor is modeled as OEIM by opening the common neutral point to get two terminals for each phase, which eases each phase to be fed through individual H-bridges. OEIM is modeled in synchronously rotating reference frame.

The dynamic model of induction motor is depicted in (30)–(33), [30]:

$$V_{\rm qs} = R_s i_{\rm mqs} + w_{\rm ms}\,(L_s i_{\rm mds} + L_m i_{\rm mdr}) + p\,(L_s i_{\rm mqs+} L_m i_{\rm mqr}) \tag{30}$$

$$V_{\rm ds} = R_s i_{\rm mds} + w_{\rm ms}\left(-L_s i_{\rm mqs} - L_m i_{\rm mqr}\right) + p\left(L_s i_{\rm mds+} L_m i_{\rm mdr}\right) \quad (31)$$

$$0 = R_r i_{\rm mqr} + \left(w_{\rm ms} - w_r\right)\left(L_m i_{\rm mds} + L_r i_{\rm mdr}\right) + p\left(L_m i_{\rm mqs+} L_r i_{\rm mqr}\right) \quad (32)$$

$$0 = R_r i_{\rm mdr} + \left(w_{\rm ms} - w_r\right)\left(-L_m i_{\rm mqs} - L_r i_{\rm mqr}\right) + p\left(L_m i_{\rm mds+} L_r i_{\rm mdr}\right) \quad (33)$$

where, $L_m$ = magnetizing inductance of the stator, $L_s$ = self-inductance of the stator, $L_r$ = self-inductance of the rotor referred to stator side, $R_s$ is stator resistance, $R_r$ is rotor resistance *d/dt* is represented as *p*, $i_{\rm mds}$ and $i_{\rm mqs}$ represent the stator *d*-axis and *q*-axis current; $i_{\rm mdr}$ and $i_{\rm mqr}$ represent the rotor *d*-axis and *q*-axis currents referred to stator, $\omega_{\rm ms}$ is the synchronous speed, and $\omega_r$ represents the motor rotor speed.

Electromagnetic torque may be expressed as follows:

$$T_e = \frac{3P}{4} L_m\left(i_{\rm mqs} i_{dr} - i_{\rm mds} i_{\rm mqr}\right), \quad (34)$$

where *p* is the number of poles.

For pump load, the load torque is expressed as (neglecting viscous friction) follows:

$$T_L = K_m {w_r}^2 + B w_r, \quad (35)$$

where *B* is viscous friction coefficient.

Neglecting viscous coefficient the load Power is expressed as cube root of speed as follows:

$$P_L = K_m {\omega_r}^3 \quad (36)$$

where $K_m$ is estimated for rated condition of the motor which is estimates as $K_m = 0.000222$. Further, the load power may be expressed in terms of motor air gap power as follows:

$$P_a = \left(\frac{\omega_r}{\omega_r + \omega_{\rm sl}}\right) P_L \quad (37)$$

where $P_a$ is air gap power, $\omega_r$ is the motor speed, and $\omega_{\rm sl}$ is the slip speed. Neglecting the losses across the stator, the air gap power is equivalent to the electrical input power fed via H-bridges. Further neglecting the losses across the bridges, the power fed by single-phase ac source as through the CMAR is as follows:

$$\frac{i_s}{2}\left(m_T + m_M + m_B\right) V_{\rm dc} = \left(\frac{r}{r + {\rm sl}}\right) K_m {\omega_r}^3 \quad (38)$$

where $i_s$ is source current and $m_j$ (where *j* is *T*, *M*, *B*) is the modulation index of the individual H-bridges. Equation (38) may be further reduced as follows:

$$\left(m_T + m_M + m_B\right) i_s K_{mt} = \left({\omega_r}^4\right) \quad (39)$$

where $K_{mt} = \frac{V_{\rm dc}}{2 \times K_m}\omega_{\rm ms}$ and $\omega_{\rm sl} + \omega_r$ is $\omega_{\rm ms}$ (synchronous frequency)

$$\sqrt[4]{\left(m_T + m_M + m_B\right) i_s K_{mt}} = \omega_r. \quad (40)$$

Actual motor speed as per (40) is governed by the reference motor speed ($\omega_r^*$), which in turn is decided based on the set reference speed ($\omega_{\rm set}$) and $\Delta\omega$ the component obtained by

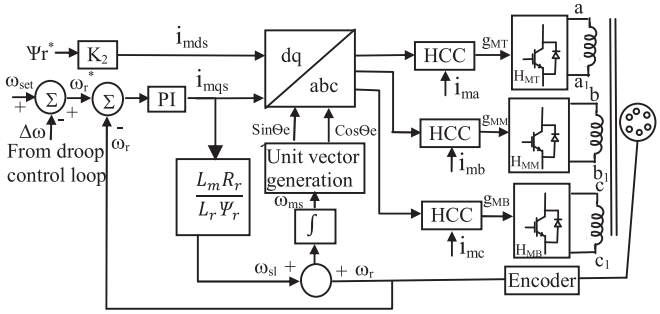


Fig. 7. Control blocks for Vector control of OEIM.

PI controller operating on error between *d* –component of the source current ($i_{\rm ds}$) and the reference current obtained through droop characteristics ($i_{\rm droop}$) as per prevailing grid frequency as in Fig. 5. Thus, the reference $\omega_r^*$ is obtained by adding $\omega_{\rm set}$ to $\Delta\omega$ to provide requisite grid support smartly to aid to the stability of the grid. With change in reference speed command, the slip speed ($\omega_{\rm sl}$) is also altered, which is given as follows:

$$\omega_{\rm sl} = \left(\frac{L_m R_r}{\Psi_r L_r}\right) i_{\rm mqs} \quad (41)$$

where $\Psi_r$ is the rated flux along *d*-axis. Further, the synchronous speed is computed by adding the $\omega_{\rm sl}$–$\omega_r$ to determine the power frequency of the motor, which in turn is used to determine the synchronizing component as shown in Fig. 7. The obtained torque and flux component ($i_{\rm mds}$, $i_{\rm mqs}$) are transformed through reverse park transformation using unit vectors to get the individual motor winding currents. These reference currents are compared with actual motor current and pass through hysteresis comparator to obtain switching command for the individual bridges. Further for pump load, any change in speed command would corroborate increase in load torque (due to its dependence on the square of speed and viscous friction), which eventually pushes the torque component ($i_{\rm mqs}$) to reach saturation limit for fast acceleration. Such sudden acceleration tends to increase $\omega_{\rm sl}$, which further increases the ($\omega_r + \omega_{\rm sl} = \omega_{\rm ms}$) synchronous speed initially, before settling it down to steady-state frequency, when speed settles to steady-state value.

## VIII. Simulation Results and Discussion

The SPL with passive load sharing the dc links having H-bridge CMAR unit at front is simulated under MATLAB Simulink environment using power system block set. To gauge the interactive action of the SPL under varying grid frequency, a programmed single-phase source with programmable frequency is created. Using e-PLL, the frequency changes are accurately tracked for proper operation of SPL using SRF-based control. The drive performance has been tested by changing the reference command for speed. The pump load on the drive is modeled using mathematical equations. For ripple free and noise less operation of vector control drive, intentionally a large size (2200 $\mu$F) having smaller voltage rating capacitor has been connected to the common dc links, shared by pair of H-bridges.

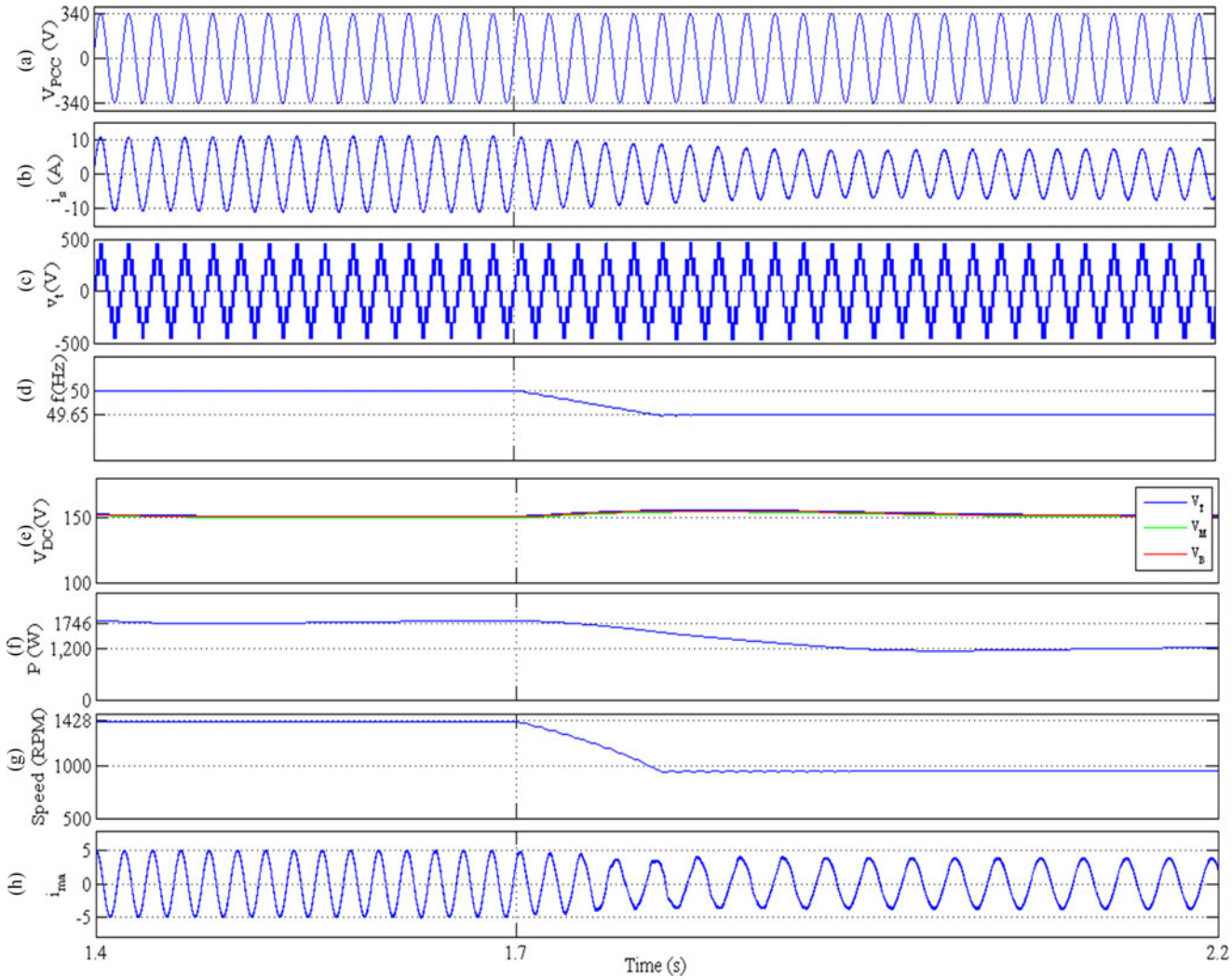


Fig. 8. Simulation waveforms of SPL unit depicting PCC voltage, source current, terminal voltage ($V_t$), grid frequency (Hz), dc link voltage, power drawn from grid by CMAR (P), motor speed (RPM), motor current ($i_{\mathrm{ma}}$).

TABLE I
PARAMETERS OF ACTIVE RECTIFIER AND INDUCTION MOTOR

| | |
|---|---|
| Main supply voltage $1\varphi$, Line Frequency | 240 V, 50 Hz |
| DC link voltages ($V_T$ , $V_M$ , $V_B$ ) | 150 V |
| DC link Capacitance | 2200 $\mu$F |
| Interface Inductor | 6 mH |
| Passive load | 966 W |
| Motor Rated Voltage, Frequency, Power | 200 V, 50 Hz, 1 Hp |
| Motor Rated Speed | 1428 RPM |
| Rotor Resistance ($R_r$ ), Stator Resistance ($R_s$ ) | 2.26, 2.7 $\Omega$ |
| Motor Mutual Inductance ($L_m$ ) | 138.4 mH |

The SPL control is verified for working with a harsh condition imposed by higher capacitance value of dc link capacitor, which may lead to PQ issues in voltage and current on grid side. The detail parameters of the active rectifying unit and OEIM are shown in Table I.

The operation of the proposed SPL unit is simulated in MATLAB Simulink and the results are shown in Fig. 8. Fig. 8. shows the waveforms for PCC voltage, which is shown maintained at 240 V ($V_{\mathrm{PCC}}$), source current ($i_s$), terminal voltage ($V_t$), frequency (f) of the grid, dc link voltage ($V_{\mathrm{DC}}$), power drawn by CMAR unit (P), motor speed (RPM) and motor phase current ($i_{\mathrm{ma}}$). The waveforms depicts steady state operation between t = 1.4 s to $t$ = 1.7 s , where it is clear that, for constant grid frequency of 50 Hz the CMAR is delivering 1746 W [see Fig. 8(f)] to VIL and pump load while maintaining dc link voltage of 150 V [see Fig. 8(e)]. From Fig. 8(g), it may be observed that motor speed remains fixed at 1428 r/min during aforesaid time period. It may also be seen in Fig. 8(b) that source current is in phase with PCC voltage conforming to UPF while maintaining a current of 7 A. At t = 1.7 s, when grid frequency is slowly reduced to 49.65 Hz as evident from Fig. 8(d), the SPL react smartly to the drop in frequency by adequately decrease in reference motor speed in accordance with droop characteristics. Accordingly, it may be observed from Fig. 8 (g) that motor speed decreases to 1200 r/min, which in turn resulted in decrease in active power demand of SPL as evident from both Fig. 8(f), which is duly confirmed by decrease in motor current from 3.5 to 2.8 A [see Fig. 8(g)] and decrease in the source current from 7 to 4.9 A

[see Fig. 8(b)]. Thus, such incorporation of the proposed control when implemented for many such SPL units together would help in the demand side management.

## IX. Hardware Setup for Experimentation

Same scale prototype using 1 HP OEIM in conjunction with 966 W VIL on different dc links is experimentally validated using requisite hardware and DSP controllers. The development of hardware includes fabrication of various control cards, interface card, voltage, and current sensor cards etc. A 415-V LEM make LV25P and 25-A ABB make EL25P1 voltage and current sensor board, respectively, are designed and fabricated using PCB designer software in conjunction with the development of PCBs for microcontrollers and its interface. The Semikron make SKM50GB063D two modules are used to construct H-bridge, and connecting such three H-bridges in cascaded configuration forms seven level of active rectifier, including 2200-μF, 250-V capacitors at each dc link of each H-bridges. The capacitor is shared by the back to back H-bridges, where one is connected with three-phase OEIM having neutral point opened to enable each phase to be connected across each H-bridge and other forms the multilevel active rectifier unit. For the indirect vector control of OEIM, speed estimation is facilitated by connecting a hollow shaft incremental encoder mounted on the motor shaft. On the very same shaft to emulate the behavior of the pump load, a fan type of load is connected. Such complete SPL unit is controlled using dSPACE 1104 real-time controller and dspic33FJ16GS502 DSP microcontroller together. The sensed parameters viz., current, voltage is feed through ADC units at sampling frequency of 9 KHz on the dSPACE 1104 board and where the speed is sensed through the incremental encoder interface available on the dSPACE board. The vector control is incorporated through hysteresis current control, where switching pulses are given though digital I/O pins available on dSPACE board.

## X. Performance Evaluation of SPL operation

The same scale developed hardware prototype is tested under perturbing static (different value of *R* loads on each dc bus) and dynamic load (three-phase induction motor pump load) and results are recorded for different condition of both balanced and unbalanced loading condition at dc buses using Agilent DSO-X 2014A oscilloscope and Fluke 345 single-phase power analyzer for evaluation of the performance of proposed SPL. The complete experimental hardware system configuration is shown in Fig. 9. At every perturbation and different point of operations of SPL, the current drawn ($i_s$) from grid always remains at UPF as shown in the trace of the oscilloscope in Fig. 10. The scaling factor for terminal voltage sensor is taken as 100:1. Moreover, for more clarity the seven-level stepped terminal voltage ($V_t$) result shown in Fig. 11 depicts the source current ($i_s$), which is in phase with PCC voltage ($V_{\rm PCC}$). Further to first check the effectiveness of the control algorithm for the proposed configuration enacting SPL even under unbalanced loading at DC buses, intentional unbalancing is created by connecting 60, 62,

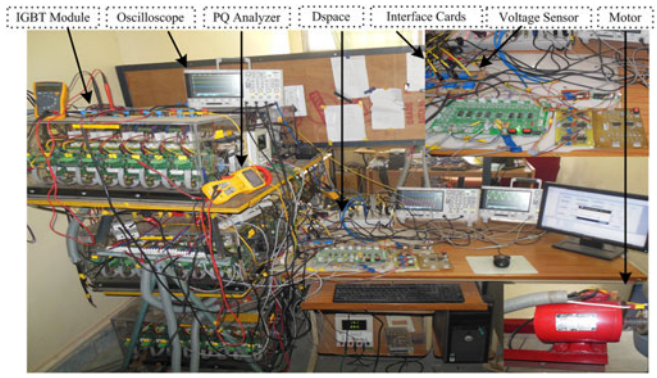


Fig. 9. Experimental setup of CMAR feeding SPL unit.

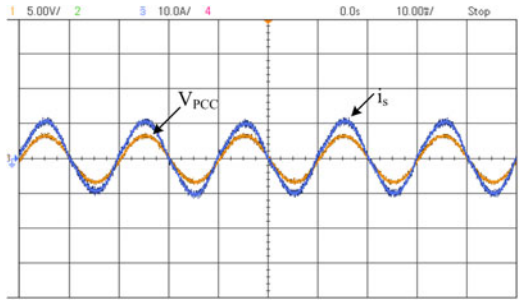


Fig. 10. Experimental result showing source voltage (500 V/div), and source current (10 A/div).

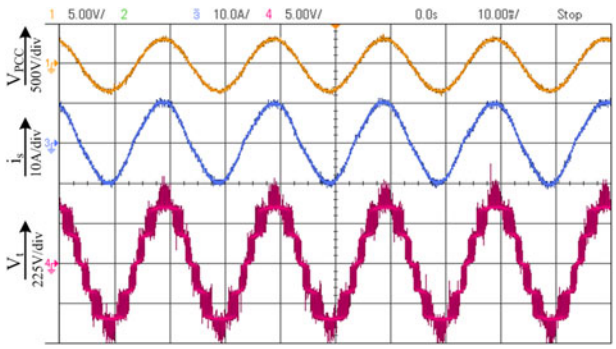


Fig. 11. Measured zoomed source voltage ($V_{\rm pcc}$), source current ($i_s$), and CMAR input voltage ($V_t$).

68 Ω passive loads across each dc link, and their voltages are recorded before and commencement of balancing control algorithm and the same is shown in Fig. 12. It is clear from Fig. 12. that at t = 2s, when balancing algorithm is started, each dc link voltage settles to 150 V, and accordingly the unbalanced static load currents gets redistributed confirming to balanced voltages on dc link.

Simultaneously triggered three oscilloscopes are employed to record the dynamics in ac source side parameters, dc bus voltages, and the motor (Pump) current and speed output, respectively in Fig. 13(a)–(c). To analyze, the performance of SPL unit is initially started with only static load as shown in Fig. 13. Till $t = 0.4$s, where SPL draws 4.1 A from source as shown in

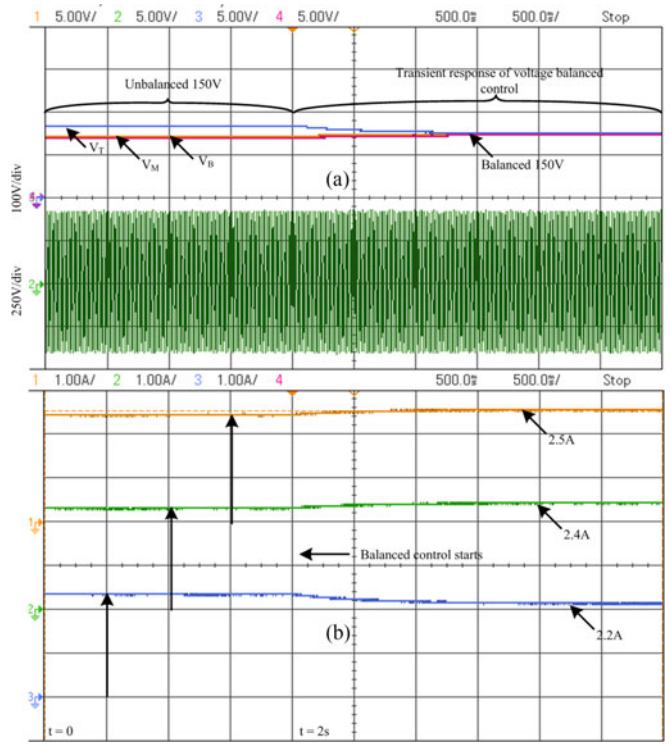


Fig. 12. Experimental results showing waveforms for dc link voltages, ($V_T$, $V_M$, $V_B$), terminal voltage and dc link load current—1 A/div under balanced/unbalanced condition.

Fig. 13(a) and the motor is not started as depicted in Fig. 13(c), where it maintains zero level till $t = 0.4$s. When OEIM is started at $t = 0.4$ s as shown in Fig. 13(c) with vector control it steadily reaches to the steady state value of 745 r/min. From Fig. 13(c), it is evident that motor current remains at the constant maximum allowable current limit to provide maximum acceleration till nearly $t = 1.5$s. In the very same time duration, it may be observed from Fig. 13(a) that source current rises from 4.1 to 5.2 A, causing small voltage dip at dc link, which recovers fast to retain back its reference voltages. A similar dip may also be seen in Fig. 13(a), where for short time dip is observed in the terminal voltage conform its connectivity to the weak grid. At $t = 4$ s another step change in speed is commanded and vector control swiftly changes the speed from 745 to 930 r/min and the transitions are also shown zoomed in Fig. 14. It may be observed that frequency gets increased to a higher value as soon as speed command is stepped up a bit higher value before settling down to the steady-state frequency, once speed gets settles in conjunction with increase in source current due to very nature of the load. The footprint of acceleration may also be observed in Fig. 13(a) in source current waveforms. Since in vector control the flux is not disturbed, but real component changes only unlike in starting case no dips in the voltage are observable. Similar dynamics has been given at $t = 10$ s.

Since the grid frequency cannot be changed at the whims and fancies of the individual, to check the effectiveness of control algorithm, the initial operating grid frequency of 50 Hz, is

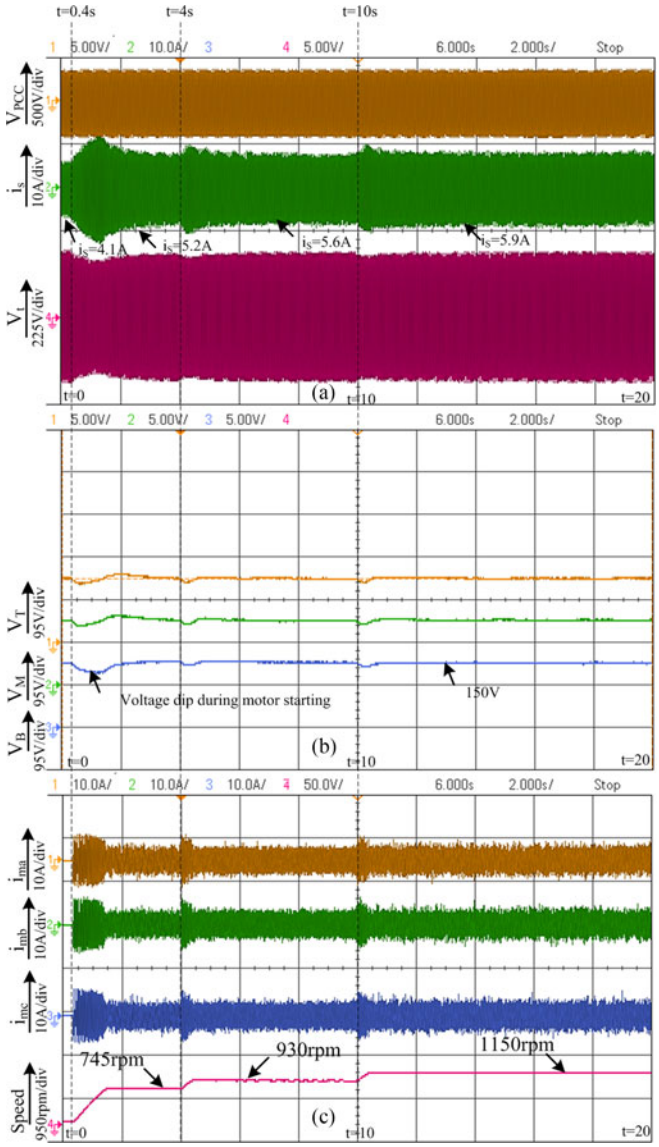


Fig. 13. Experimental results showing (a) source voltage ($V_{\rm pcc}$), source current ($i_s$), and CMAR input voltage ($V_t$). (b) DC link voltages ($V_T$, $V_M$, $V_B$). (c) Motor currents ($i_a$, $i_b$, $i_c$), motor speed.

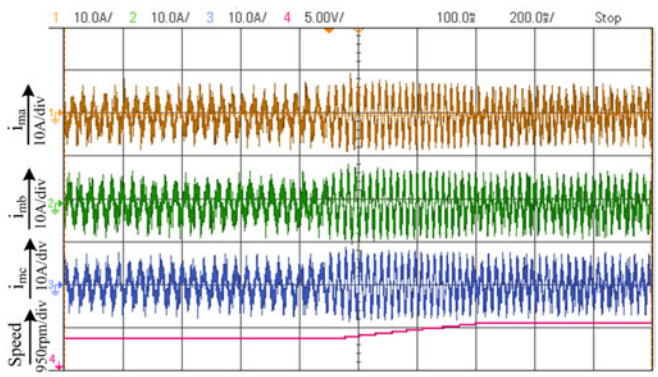


Fig. 14. Experimental results showing zoomed motor current $i_{\rm ma}$, $i_{mb}$, $i_{mc}$, and speed.

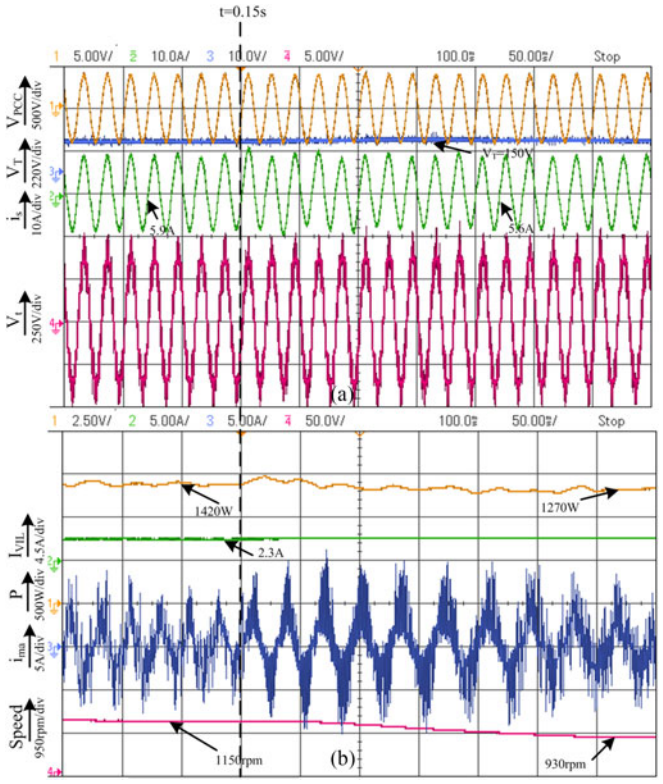


Fig. 15. Experimental result showing (a) source voltage ($V_{\rm pcc}$), dc link voltage, source current ($i_s$), and CMAR terminal voltage ($V_t$), (b) power drawn by CMAR (P), VIL current ($I_{VIL}$), motor current ($i_{\rm ma}$), and speed.

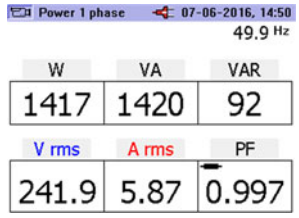


Fig. 16. Screenshot of a power analyzer.

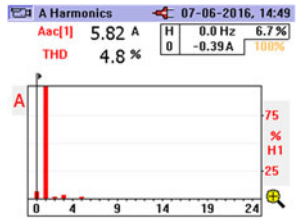


Fig. 17. Screenshot of THD of source current harmonics.

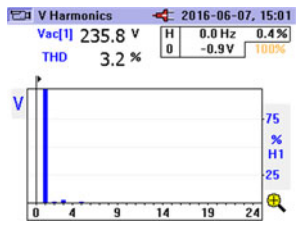


Fig. 18. Screenshot of THD of CMAR terminal voltage $V_t$.

assumed altered at $t = 0.15$s to 49.65 Hz by altering the $P_{\rm droop}$ reference in accordance with the droop characteristics. This changed $P_{\rm droop}$ accordingly commands the change in speed as per the designed control scheme to account for offsetting the burden. Accordingly, at $t = 0.15$ s, the controller prescribe a new reference command making the motor speed swiftly dropped to 930 r/min from 1150 r/min in turn reducing the frequency of the motor currents from 40 Hz to 28.8 Hz as clearly evident in the simultaneously triggered oscilloscope traces shown in Fig. 15(b). Such reduction in speed reflected in reduction of the total power drawn from grid from 1420 to 1270 W, maintaining VIL current same at 2.3 A shown in Fig. 15(b). Moreover, such reduction in speed resulted in reduction of overall source current demanded by SPL unit from 5.9 to 5.6 A [see Fig. 15(a)]. Meanwhile, the dc link voltage remains maintained at 150 V as shown in Fig. 15(a). Such multiple units of SPL if used on rural distribution grid prompts to reduction of the overall loads smartly with grid frequency and would in turn reduce the net demand on the grid, contributing to the stability of the grid.

A snapshot of Fluke 345 power analyzer is shown in Fig. 16 depicting power drawn by SPL prototype unit when the motor is running at 1240 r/min. From snapshot, it is further clearly illustrated that source current is maintained at UPF with current magnitude of 5.87 A. Figs. 17 and 18 show the THD of source current and terminal voltage, which is well within limits (4.8% and 3.2%, respectively) conforming to the IEEE 519 standards.

## XI. Conclusion

The new concept of SPL using power electronics hardware for splitting single-phase supply to three-phase utilizing CMAR for vector control of three-phase OEIM and other passive loads on its three different dc buses (balanced/unbalanced) is demonstrated through both by simulation and experimental results for grid interactive operation with improved PQ. The effectiveness of the droop control algorithm under low-grid frequency conditions is clearly demonstrated through results by fast vector operation control operation of OEIM. CMAR always draw current from grid at unity power factor ensuring improved PQ operation. Further, keeping the entire voltages on the dc buses constant and balanced ensures smooth operation of smart pump drive immune to the disturbance both from ac or dc side. The control algorithm in *d–q* frame ensures immunity to any noise and harmonics in voltage at PCC. The proposed algorithm operates in conjunction with grid and enjoys the advantage of modularity, high efficiency for feeding SPLs, and other passive loads connected on dc buses. The proposed configuration has the advantage of small voltage rating capacitor, which guarantees the extended life and also provides ride through capability ensuring smooth operation of smart pump drive for cooperative operation with the grid. The SPL also helps in reduction of the dv/dt stress on the switches and also reduces the heat dissipation across the devices, besides strengthening the stability of the grid by providing adequate demand side management. Such

multiple units acting together smartly would strengthen the grid even under the influence of integrated low inertia sources.

## REFERENCES


[1] J. Liu, Y. Miura, and T. Ise, "Comparison of dynamic characteristics between virtual synchronous generator and droop control in inverter-based distributed generators," *IEEE Trans. Power Electron.*, vol. 31, no. 5, pp. 3600–3611, May 2016.

[2] P. J. Douglass, D. Lyngby, R. Garcia-Valle, P. Nyeng, and J. Ostergaard, "Smart demand for frequency regulation: Experimental results," *IEEE Trans. Smart Grid*, vol. 4, no. 3, pp. 1713–1720, Jul. 2013.

[3] J. Liu, Y. Miura, and T. Ise, "Comparison of dynamic characteristics between virtual synchronous generator and droop control in inverter-based distributed generators," *IEEE Trans. Power Electron.*, vol. 31, no. 5, pp. 3600–3611, May 2016.

[4] Q. Jia, J. Shen, Z. Xu, and X. Guan, "Simulation-based policy improvement for energy management in commercial office buildings," *IEEE Trans. Smart Grid*, vol. 3, no. 4, pp. 2211–2223, Dec. 2012.

[5] Y. J. Kim, L. K. Norford, and J. L. Kirtley, "Modeling and analysis of a variable speed heat pump for frequency regulation through direct load control," *IEEE Trans. Power Syst.*, vol. 30, no. 1, pp. 397–408, Jan. 2015.

[6] P. N. Enjeti and A. Rahman, "A new single-phase to three-phase converter with active input current shaping for low cost AC motor drives," *IEEE Trans. Ind. Appl.*, vol. 29, no. 4, pp. 806–813, Jul. 1993.

[7] H. Zhong, L. Zhao, and Y. Zhang, "Dynamic performance analysis of novel series-connected capacitor-run three-phase induction motor fed by single-phase supply," in *Proc. 2014 IEEE Transp. Electrific. Conf. Expo.*, Dearborn, MI, USA, 2014, pp. 1–6.

[8] M. M. Swamy and C. Guddanti, "An improved single-phase active-front-end rectifier system for use with three-phase variable-frequency drives," *IEEE Trans. Ind. Appl.*, vol. 51, no. 2, pp. 1732–1742, Sep. 2014.

[9] O. Ojo, S. Asuri, G. Dong, and Z. Wu, "Control of an induction motor drive fed with a single-phase fed sparse PWM rectifier/inverter," *Proc. IEE Elect. Power Appl.*, vol. 152, no. 3, pp. 526–534, May 2005.

[10] D.-C. Lee and Y.-S. Kim, "Control of single-phase-to-three-phase AC/DC/AC PWM converters for induction motor drives," *IEEE Trans. Ind. Electron.*, vol. 54, no. 2, pp. 797–804, Apr. 2007.

[11] C. B. Jacobina and E. C. dos Santos Jr., "Single-phase to three-phase drive system using two parallel single-phase rectifiers," *IEEE Trans. Power Electron.*, vol. 25, no. 5, pp. 1285–1295, Jan. 2010.

[12] Y. Son and J.-I. Ha, "Direct power control of a three-phase inverter for grid input current shaping of a single-phase diode rectifier with a small DC-link capacitor," *IEEE Trans. Ind. Appl.*, vol. 7, no. 30, pp. 3794–3803, Aug. 2014.

[13] S. Jain, R. Karampuri, and V. T. Somasekhar, "An integrated control algorithm for a single-stage PV pumping system using an open-end winding induction motor," *IEEE Trans. Ind. Electron.*, vol. 63, no. 2, pp. 956–965, Feb. 2016

[14] J. Arribas and C. González, "Optimal vector control of pumping and ventilation induction motor drives," *IEEE Trans. Ind. Electron.*, vol. 49, no. 4, pp. 889–895, Aug. 2002.

[15] H. Akagi and S. Tamura, "A passive EMI filter for eliminating both bearing current and ground leakage current from an inverter-driven motor," *IEEE Trans. Power Electron*., vol. 21, no. 5, pp. 1459–1469, Sep. 2006.

[16] V. T. Somasekhar, K. Gopakumar, M. R. Baiju, K. K. Mohapatra, and L. Umanand, " A multilevel inverter system for an induction motor with open-end windings," *IEEE Trans. Ind. Electron.*, vol. 52, no. 3, pp. 824–836, Jun. 2005.

[17] A. Edpuganti and A. K. Rathore, "New optimal pulse width modulation for single DC-link dual-inverter fed open-end stator winding induction motor drive," *IEEE Trans. Power Electron.*, vol. 30, no. 8, pp. 4386–4393, Aug. 2014.

[18] I. Çadirci, G. Akçam, and M. Ermis, "Effects of instantaneous power-supply failure on the operation of slip-energy recovery drives," *IEEE Trans. Energy Convers.*, vol. 20, no. 1, pp. 7–15, Mar. 2005.

[19] J. A. Barrena, L. Marroyo, M. A. R. Vidal, and J. R. T. Apraiz ,"Individual voltage balancing strategy for PWM cascaded H-bridge converter-based STATCOM," *IEEE Trans. Ind. Appl.*, vol. 55, no. 1, pp. 21–29, Jan. 2008.

[20] C. Cecati, A. Dell Aquila, M. Liserre, and V. G. Monopoli, "Design of H-bridge multilevel active rectifier for traction systems," *IEEE Trans. Ind. Appl.*, vol. 39, no. 5, pp. 1541–1550, Sep. 2003.

[21] Y. Liu, A. Q. Huang, W. Song, S. Bhattacharya, and G. Tan, "Small-signal model-based control strategy for balancing individual DC capacitor voltages in cascade multilevel inverter-based STATCOM," *IEEE Trans. Ind. Electron.*, vol. 56, no. 6, pp. 2259–2269, Jun. 2009.

[22] L. K. Haw, M. S. A. Dahidah, and H. A. F. Almurib, "SHE–PWM cascaded multilevel inverter with adjustable DC voltage levels control for STATCOM applications," *IEEE Trans. Power Electron.*, vol. 29, no. 12, pp. 6433–6444, Dec. 2014.

[23] J. Napoles, J. I. Leon, and R. Portillo, "Selective harmonic mitigation technique for high-power converters," *IEEE Trans. Ind. Electron.*, vol. 57, no. 7, pp. 2315–2323, Jul. 2010.

[24] H. Kim and K.-H. Kim, "Filter design for grid connected PV inverters," in *Proc. IEEE Int. Conf. Sustainable Energy Tech.*, 2008, pp. 1070–1075.

[25] B. Singh and V. Verma, "Selective compensation of power-quality problems through active power filter by current decomposition," *IEEE Trans. Power Del.*, vol. 23, no. 2, pp. 792–799, Apr. 2008.

[26] R. Naderi and A. Rahmati, "Phase-shifted carrier PWM technique for general cascaded inverters," *IEEE Trans. Power Electron.*, vol. 23, no. 3, pp. 1257–1269, May 2008.

[27] A. A. A. Radwan and Y. A. R. I. Mohamed, "Stabilization of medium-frequency modes in isolated microgrids supplying direct online induction motor loads," *IEEE Trans. Smart Grid*, vol. 5, no. 1, pp. 358–370, Jan. 2014.

[28] Central Electricity Regulatory Commission, New Delhi, India [Online]. Available: http://cercind.gov.in/2014/regulation/reg21.pdf

[29] A. Kumar, D. Kumar, and D. R. Meena, "SRF based modeling and control of cascaded multilevel active rectifier with uniform DC-buses," in *Proc IEEE Int. Conf. Recent Adv. Eng. Comput. Sci.*, 2014, pp. 1–5.

[30] R. Krishnan,*Electric Motor Drives: Modeling, Analysis, and Control*, 1st. ed. *Englewood Cliffs, NJ, USA*: *Prentice-Hall*, 2001, pp. 196–219.


**Vishal Verma** (M'04) received the B.Tech. degree from G.B. Pant University, Pantnagar, India, and the M.Tech. and Ph.D. degrees from the Indian Institute of Technology, New Delhi, India. In 1991, he joined the Department of Electrical Engineering, G.B. Pant University, as an Assistant Professor and later in 2004, joined the Delhi College of Engineering (Now Delhi Technological University), Delhi, India, where he became a Professor in 2009.

He is currently serving as a Full Professor in the Department of Electrical Engineering and Dean Academics (PG). He is a Member of ISTE and a Life Member of CES(I). His field of interest includes power electronics, power-quality issues, grid integration of renewable energy sources, and ac–dc microgrids.

**Amritesh Kumar** received the B.Tech. degree in electrical and electronics engineering from SASTRA University, Thanjavur, India, in 2009 and the M.E. degree in power electronics and drives from BITS Pilani, Pilani, India, in 2011. He is currently working towards the Ph.D. degree in the Department of Electrical Engineering, Delhi Technological University, Delhi, India, in the field of power electronics.

His main research interests are analysis and design of power converters and its application in renewable energy, drives, multilevel inverters, and active filters.